Results in Surfaces and Interfaces 12 (2023) 100132

Contents lists available at ScienceDirect

Results in Surfaces and Interfaces

journal homepage: www.elsevier.com/locate/rsurfi

Hydrophobicity and icephobicity of micropillared silicone rubber surfaces fabricated by compression molding

S. Keshavarzi *, B. Bouazara, G. Momen, R. Jafari

Department of Applied Sciences, University of Québec in Chicoutimi, Chicoutimi, Québec, G7H 2B1, Canada

ARTICLE INFO

Keywords:
Micromachining
Compression molding
Pillar array
Hydrophobicity
Geometry
Ice nucleation time

ABSTRACT

This study investigates the effects of microcylindrical pillar geometry on surface wettability and ice nucleation time. The cylindrical micropillars were designed and then fabricated on silicone rubber surfaces by micromachining to create a template, followed by direct replication using a compression molding method. This approach offers an efficient, nontoxic, and low-cost means of producing micro-nanoscale roughness on surfaces. We tested the wetting (i.e., contact angle and contact angle hysteresis) and anti-icing (i.e., ice nucleation time) properties of the patterned silicone rubber surfaces having different combinations of pillar diameter and interpillar spacing. According to our experimental results for a limited range of pillar diameters (80 and 110 μm) and center to center spacing (pitch; 125–300 μm), decreasing the diameter and increasing the space of micro-cylindrical pillars may result in the Cassie wetting until a threshold value. Beyond this pillar diameter/pitch threshold, Wenzel wetting occurred. Surfaces characterized by pillars of different diameter and pitch also increased the freezing delay by reducing the area of ice–substrate contact and the heat transfer between the water droplet and the surface. We demonstrate that the properties of superhydrophobic and anti-icing surfaces can be controlled by altering the geometry of micropillars across the surface.

1. Introduction

Superhydrophobic materials offer a promising anti-icing technology for use in, among other, self-cleaning, drag reduction, corrosion prevention, and fog prevention applications (Robin H.A. Ras, 2016; Zhang et al., 2008; Guo and Yang, 2018; Jiang et al., 2022). The water repellency of these materials makes them effective at preventing the icing of water droplets and reducing ice adhesion on surfaces (Shen et al., 2019; Tourkine et al., 2009; Hou et al., 2020a). Surface hydrophobicity is generally determined by measuring the contact angle between water droplets and the surface, and two wetting states govern liquid droplet behavior on rough surfaces: Cassie–Baxter and Wenzel states. In a Cassie–Baxter state, a liquid droplet is suspended on top of a rough surface with air trapped in the underlying hollow spaces. In contrast, the Wenzel state wets the solid substrate by filling the space between the surface grooves (Robin H.A. Ras, 2016; Cassie and Baxter, 1944; Wenzel, 1949).

Well-arranged micro/nanostructures having a low energy surface can produce superhydrophobic behavior with contact angles (CA) >150° and a contact angle hysteresis (CAH) of <10° (Jeevahan et al., 2018; Bhushan et al., 2007). Superhydrophobic surfaces can be produced on a variety of materials (Bhushan and Chae Jung, 2007). Thermoplastic has been used as a matrix for fabricating superhydrophobic polymeric surfaces, and other researchers have combined poly(dimethylsiloxane) (PDMS) and liquid silicone rubber (LSR) to produce structured superhydrophobic surfaces (Hopmann et al., 2014; Nayak et al., 2013; Gao et al., 2016; Aldhaleai and Tsai, 2021; Maghsoudi et al., 2018). High-temperature vulcanized (HTV) silicone rubber materials can also be used to create textured superhydrophobic surfaces. The hydrophobic properties of silicone rubber have led to its use as high-voltage outdoor insulation (Maghsoudi et al., 2018, 2020a). In cold environments, the hydrophobic properties of silicone rubber diminish gradually, and moisture and pollutants can adsorb onto its surface. The silicone rubber insulator will thus be exposed to a higher risk of flashover, especially when subjected to surface icing (Farzaneh, 2014); thus, improvements must be made to silicone rubber surfaces to increase their icephobicity. The smooth surface of an unmodified silicone rubber produces a water contact angle of <120°; however, adding surface roughness can increase the CA without altering the surface chemistry.

Micro- and nanostructured superhydrophobic surfaces can be created through a variety of techniques, including self-assembly, layer-by-layer methods, plasma treatments, chemical vapor deposition, sol–gel methods, lithography, spray coating, dip coating, electrostatic spinning, and electrochemical deposition (Subhash Latthe et al., 2012; Ma and Hill, 2006; Hu et al., 2015). When these methods are used in real-world settings, several challenges and problems emerge, including complex

* Corresponding author.
E-mail address: samaneh.keshavarzi1@uqac.ca (S. Keshavarzi).

https://doi.org/10.1016/j.rsurfi.2023.100132
Received 12 April 2023; Received in revised form 10 July 2023; Accepted 12 July 2023

engineering procedures, long fabrication times, expensive facilities, unsuitability for different materials, a low removal rate of material, environmental concerns, and less than optimal substrate robustness (Gao et al., 2016; Maghsoudi et al., 2018; Pratap and Patra, 2018). Therefore, a simpler approach using micromachining – to create the microholes – and compression molding – to generate replicas having micro- or nanostructures – can reduce fabrication time and costs, be applied to a wide range of materials, and be highly reproducible. Moreover, mass production methods, like using templates as replicas to create micro-nanostructured surfaces, are generally accepted and commonly used in industry. Another advantage of direct replication is creating a superhydrophobic surface directly out of the bulk material, whereas existing techniques must add an additional layer to change surface wettability (Pratap and Patra, 2018; Liu et al., 2009; Maghsoudi et al., 2020b). Fabricating these micro-nanostructures on templates is commonly performed using photolithography and laser techniques (Nayak et al., 2013; Öner and McCarthy, 2000). These approaches have many advantages, but they are also costly, time-consuming, and difficult to implement in large-area industrial applications. Another alternative approach for fabricating a mold insert with micropillar arrays and nanopillars on its surface involves combining an anodic aluminum oxide template with an etched plate (Zhou et al., 2018; Weng et al., 2019; Brousseau et al., 2010). Although this method offers a simplified and cost-effective approach with high production rates, it is limited in design flexibility and the availability of suitable templates. Mechanical machining via a focused ion beam (FIB), incremental stamping, and molding can also produce precise and flexible templates; however, this involves more process steps, longer production times, and potential limitations in design reproduction (Matsumura et al., 2012). These techniques have been explored extensively in the literature, and although they have contributed valuable insights into surface engineering and superhydrophobicity, there remains a need for alternative approaches that address the existing practical challenges and provide accessible solutions for industrial applications. In light of these considerations, we selected computer numeric control (CNC) to fabricate patterned templates, streamline the process, and facilitate large-scale production.

Microstructure geometry affects wettability and icephobicity. For example, Gao et al. (2016) investigated the surface hydrophobicity of patterned pillars on intrinsically hydrophobic PDMS and a hydrophilic SU-8 silicon wafer. Their wetting experiments of PDMS pillar arrays demonstrated that the Cassie-to-Wenzel transition occurs as pillar spacing increases. The intrinsically hydrophilic surface (SU-8), however, produced smaller CAs without changing wetting states. The difference in the material wetting response stems from the inherent wettability of each polymer. A bio-inspired texture geometry was investigated by He et al. (2014) to understand the role of geometry in affecting wettability and ice adhesion. Compared with a smooth surface lacking structure, the surface with hierarchical micro-nanopillars had a lower ice adhesion, as the surface geometry limited the contact area between ice and substrate and thus reduced ice adhesion. He et al. (2013) also investigated the relationship between microstructure geometry and wetting state transitions. Using a micro-square rod model to control surface wettability – without considering chemical interactions and different geometric parameters – they found that increasing micro-rod height and decreasing micro-rod spacing produced a Cassie wetting state, whereas decreasing micro-rod height and increasing the spacing favored a Wenzel wetting state. Finally, a laser-based modification of a silicon silicone rubber surface led to increased CAs and decreased ice adhesion strength as roughness and the root mean square slope of the silicone rubber surface increased (Chen et al., 2018, 2020).

Despite these studies of how surface morphology affects surface wettability and icephobicity, little research has tested the effects of geometrical parameters, including pillar pitch and the diameter of silicone rubber surfaces. Moreover, it is critical to control the microstructures of silicone rubber surfaces to maintain the hydrophobic and icephobic properties of silicone rubber at low temperatures to ensure the practical application of silicone rubber insulation products.

Here, we investigate how the geometrical parameters of patterned silicone rubber surfaces with cylindrical pillars of varying diameter and pitch (pillar center-to-center distance) affect the CA, CAH, and ice nucleation time of silicone rubber surfaces. We apply microfabrication technology using CNC and compression molding because of the ease of controlling geometric parameters. We also study surface icing to explore the role of geometrical parameters of the designed microstructures on icing delay.

2. Materials and methods

HTV silicone rubber was used as the supporting substrate. We propose a periodic microcylindrical model with various geometrical parameters to control surface wettability. The details of template fabrication and the applied direct replication processes to produce the micropillared surfaces are explained in the following sections.

2.1. Fabrication of templates

An MDX 540 computer numeric control (CNC) machine created the microholes on a mask. In addition to achieving different homogeneous and ordered textures, this tool can also produce very low distension values between the holes and produce holes having micrometric diameters. To engrave microholes on an aluminum substrate, we used Fusion 360 software to design the desired microstructure; the design was then converted into G-code for the CNC machine. We fabricated cylindrical structures with various hole diameters (D), center-to-center spacing (pitch; P), and height (H) (Fig. 1).

2.2. Replication process

We used HTV silicone rubber as the bulk material and a compression machine (Carver Inc., USA) to replicate the structures on the silicone rubber (Fig. 2). A control panel controlled the hydraulic press and thermostat on the compression machine. The hydraulic press applied force to the two platens of the machine, and the thermostat controlled the heating of the platens. Rubber materials were cast in a three-piece flat mold with cavity dimensions of 25 × 25 × 6.5 mm. In the cavity, we carefully placed the template. An anti-stick coating was applied to all templates to enhance replication quality; for this we used diluted TPFS (Trichloro(1H,1H,2H,2H-perfluorooctyl)silane) in methanol (Maghsoudi et al., 2018). After placing the silicone rubber into the cavity, we fastened three pieces of the mold together and placed them on the platen of the press machine set at 160 °C. A hydraulic pump was then used to press the two platens closer together until the desired pressure was reached (4.3 MPa). To cure the rubber completely, we kept the platens closed. The platens were opened after six minutes, and the cured rubber was demolded.

2.3. Surface characterization

We measured the CA and the CAH of the HTV silicone rubber surface using a Kruss™ DSA100 goniometer equipped with a video camera. We measured the static CA by depositing a 4 μL water droplet on the surface. The CA was then calculated using the Young–Laplace approximation. As the water droplet moved across the surface, we determined the dynamic contact angle (CAH) by measuring the advancing and receding contact angles. The CA of each sample was measured at five different points on the sample under conditions of 22 °C and −20 °C, at 30% relative humidity, to ensure measurement accuracy and reproducibility. We reported the average CA and standard deviation for each sample.

Patterned morphology of the silicone rubber surfaces was observed using a scanning electron microscope (JSM-6480 LV SEM, manufactured by JEOL, Japan). To assess replication quality, we used an optical profiler (Profil3D, Filmetrics, USA) to quantify the cylindrical pattern of the surface.

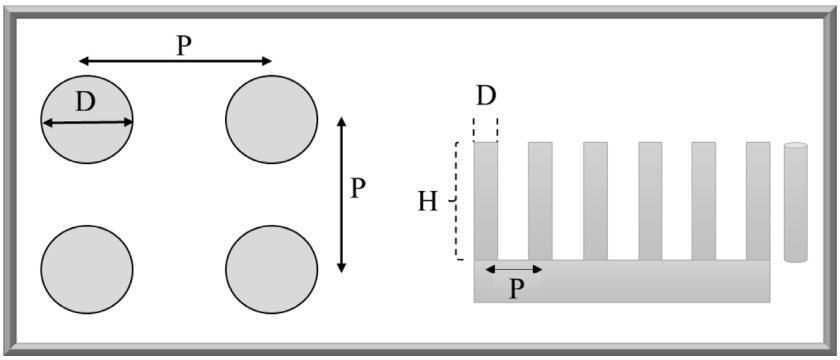

Fig. 1. Creation of microholes (D, hole diameter; P, pitch: center-to-center spacing; H, hole height).

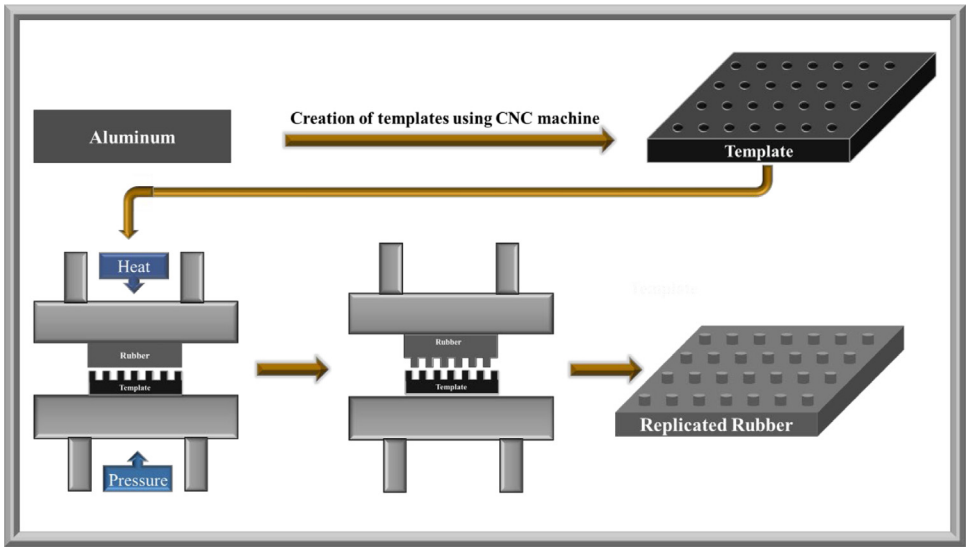

Fig. 2. A schematic of the replication of micropillars on the HTV silicone rubber.

2.4. Experimental setup

On a lab-built setup, schematically shown in Fig. 3, we conducted the surface icing experiments on the microstructured silicone rubber surfaces. Our setup included a thermally insulated and optically transparent chamber, a high-speed camera, a thermostatic bath, a cold base, drop injection, test samples, a data acquisition system, a temperature sensor, a humidity sensor, and a vibration-free table. The double-layered, thermally insulated, and optically transparent chamber allowed an accurate and reproducible means of controlling temperature and humidity so that only select parameters affecting ice nucleation were altered, and the ambient conditions remained almost uniform throughout the experiment.

To measure ice nucleation time, we placed the as-processed silicone rubber surfaces onto a cold base. A thermocouple (K-type) was used to detect and control the cooler's temperature. A 10 μL water droplet was carefully placed on the surface using a droplet injection system and cooled to −20 °C. A high-speed camera (MotionBLITZ, MIKROTRON, EoSens Cube 7, Germany) captured the nucleation and freezing processes.

3. Results and discussion

3.1. Morphology and microstructure of a compression molding–patterned silicone rubber surface

Using micromachining via the CNC machine, we created 13 different ordered templates on the aluminum substrate in two series of microholes (Fig. 4). The produced microholes had dimensions of D = 80 ± 5 μm, P = 125, 150, 175, 200, and 225 μm, and H = 85 ± 5 μm for Series 1 and D = 110 ± 5 μm, P = 125, 150, 175, 200, 225, 250, 275, and 300 μm, and H = 85 ± 5 μm for Series 2.

Fig. 5 presents SEM images of the patterned microstructures on silicone rubber produced via compression molding and the cylindrical pillars of variable geometrical parameters designed using Fusion 360. The software controlled precisely pillar diameter and spacing, whereas pillar height could be adjusted using the thickness of aluminum template. We used the same aluminum thickness to produce microstructure heights of equal height for all surfaces. To examine the morphologies of silicone rubber surfaces after compression molding, we examined their 3D profiles using an ultra-depth 3D microscope (Fig. 6). These profiles confirm the successful fabrication of patterned microstructures on the silicone rubber substrates; the cylindrical pillars had a height of about 85 ± 5 μm. We measured pillar heights directly in SEM and via the profilometry images of silicone rubber surfaces. The pillar tops were observed with a higher magnification and showed a microscale roughness (S_q, root mean square roughness) of 1.724 μm.

3.2. Surface wettability

Water contact angle served to assess surface wettability of the samples (Fig. 7). Pristine silicone rubber surface has a water CA of 116°, making it hydrophobic. Adding pillars to the surface increases the water CA, leading to a greater hydrophobicity of the prepared silicone rubber surfaces than the original smooth surfaces.

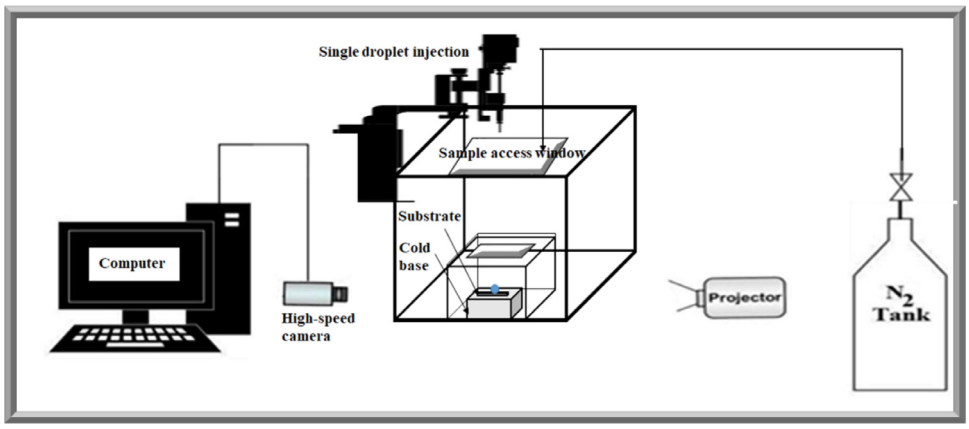

Fig. 3. Schematic of the experimental setup (Keshavarzi et al., 2022b).

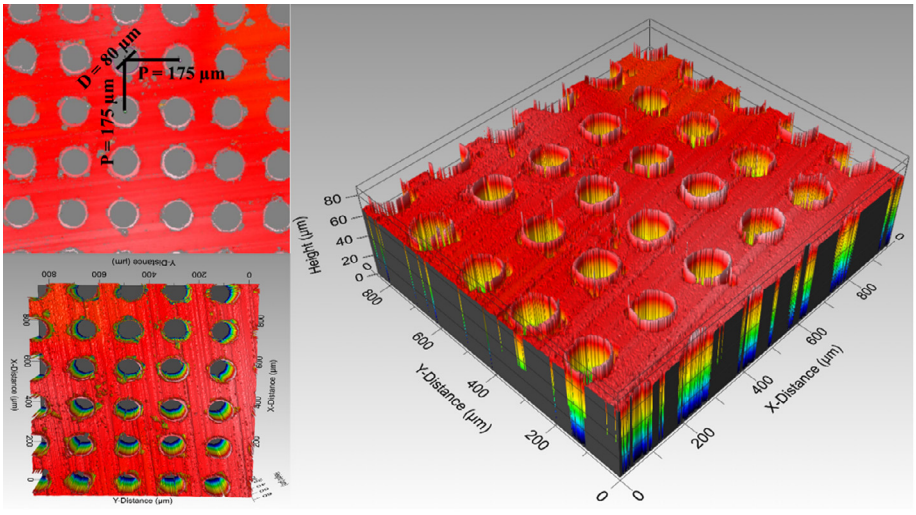

(a)

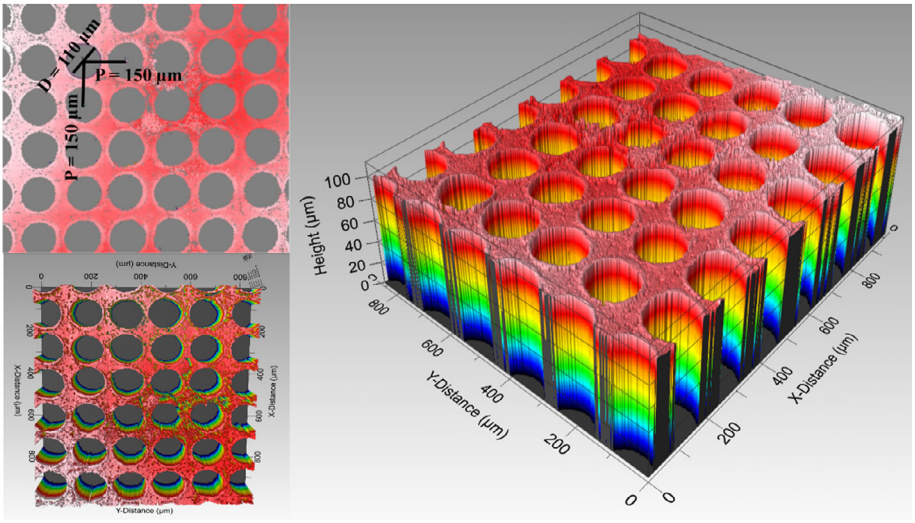

(b)

Fig. 4. Microholed surfaces fabricated using a CNC machine; a micropillar-covered surface with pillar dimensions of (a) $D = 80 \pm 5$ µm, $P = 175 \pm 3$ µm and (b) $D = 110 \pm 5$ µm, $P = 150 \pm 3$ µm.

When pillar diameter is 80 µm, the CA are all close to 150°, and the CAH is generally <10° (Fig. 7c). These surfaces therefore demonstrate superhydrophobic behavior and display a Cassie wetting state. For a pillar diameter of 110 µm, CA are all <150° (Fig. 7b), and the hysteresis is between 16° and 25° (Fig. 7d), indicating a lower surface hydrophobicity for the larger-diameter pillars. As the pitch increases from 125 to

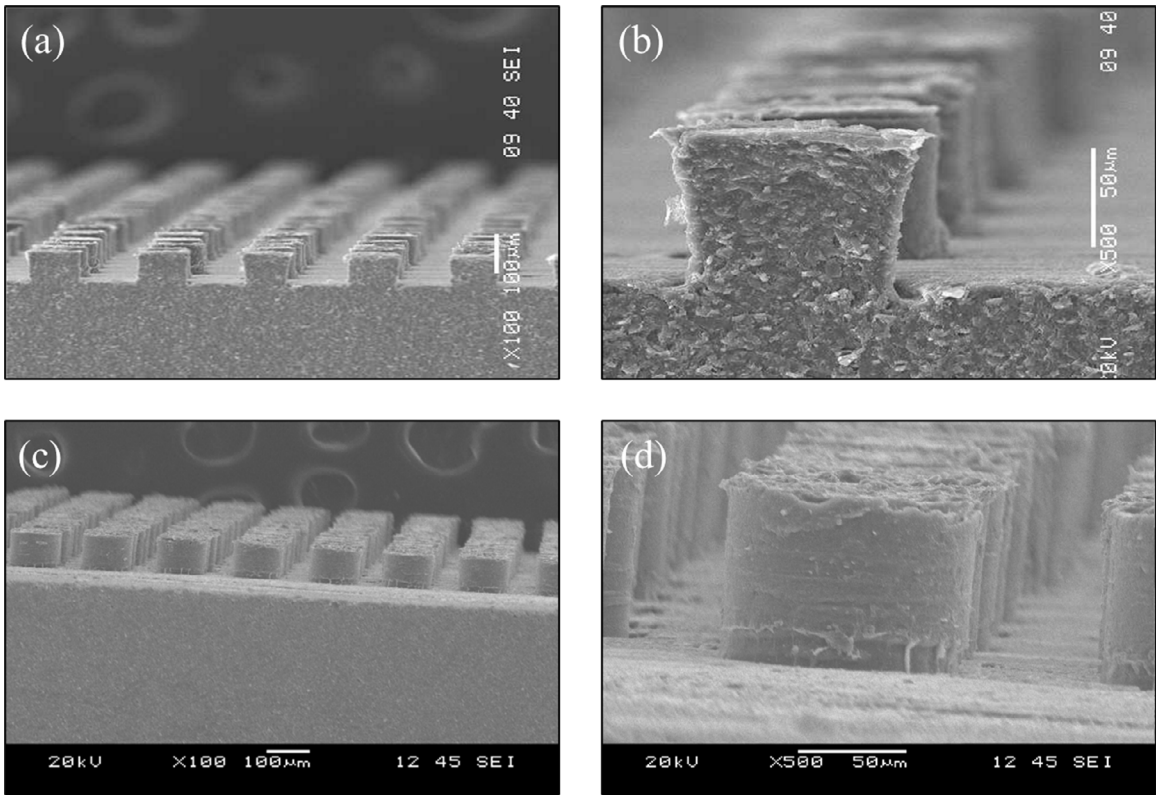

Fig. 5. SEM images of microstructures with parameters of D = 80 µm and P = 175 µm at a magnification of (a) 100× and (b) 500×; and microstructures with parameters of D = 110 µm and P = 150 µm at a magnification of (c) 100× and (d) 500×.

225 µm for the micropillared surfaces, CA increases from 136° to 149° (Fig. 7b). The CAH decreases as the pitch increases, indicating that the micropillars reduce surface wettability. Increasing pitch distance (P) creates more air pockets between pillars, which prevents water droplets from penetrating between the micropillars (Gao et al., 2016; He et al., 2013). As the inter-micropillar distance increases beyond 225 µm, CA decreases; for example, at a 300 µm center-to-center spacing distance, the CA is 140°. A greater distance between micropillars can cause the Cassie–Baxter wetting state to become unstable. With a larger distance between micropillars, droplets embedded in the microstructures have a lower CA. According to Extrand (Extrand, 2004) and Gao (Gao et al., 2016), surface tension causes a droplet to lift upward when suspended on the top of rough features of a hydrophobic surface (Cassie–Baxter wetting). Droplets are supported by this force against gravity. When the interpillar distance increases, the surface tension force decreases because there are fewer pillars underneath the water droplet. In the case of the surface tension force that is smaller than the droplet weight, Cassie wetting no longer occurs, and water droplets fall into asperities on the surface.

Increasing the micropillar diameter causes a transition from a Cassie–Baxter to a Wenzel state and thus a change in hydrophobicity. The wetting state can therefore be controlled by altering the geometry of micropillars on the silicone rubber surface, and superhydrophobicity can be produced using silicone rubber microstructures without any additional coatings or treatments. Wenzel wetting is produced by increasing pillar diameter and the increasing spacing between the micropillars above a threshold, whereas Cassie–Baxter wetting occurs as the pillar diameter decreases and inter-micropillar spacing increases until a threshold (Bhushan et al., 2007).

Gao et al. (2016) examined the effect of circular pillar arrays fabricated by lithography on PDMS and SU-8 hydrophobicity . They investigated 45 µm high pillars of various diameters (25, 35, 45, and 55 µm) and interpillar spacing (20–200 µm). The CA initially increased with increasing pillar spacing, followed by a decrease beyond a critical spacing distance, consistent with our findings regarding the influence of pitch on CA. Similarly, He et al. (2013) studied the hydrophobicity of silicon wafers with microsquare rods fabricated by lithography. Their observations of CA and CAH in relation to pillar height (20 and 40 µm) and spacing (10–160 µm) are also consistent with our observations on the influence of pillar diameter and pitch.

Our observations regarding the impact of pitch on CA and CAH are also supported by the study of He et al. (2014), who investigated the role of bio-inspired texture geometry on wettability. Their study of micropillars topped with nanopillars demonstrated that hydrophobic surfaces have a greater CA and lower CAH as micro-nanopillar spacing increases.

Hou et al. (2020b) applied selective plasma etching technology to create a series of microcubic arrays on a silicon surface. The designed micropillars varied in their spacing (30–130 µm) on the silicon surface, and the microcubic arrays were designed with an edge length equal to pillar height (20 µm). They observed a transition from a Cassie wetting state to a Wenzel wetting state as the spacing between micropillars increased, a transition similar to our observations of a shift from a Cassie to a Wenzel wetting state with increased pitch.

In summary, our findings for HTV silicone rubber support previous research on various materials to highlight the influence of surface microstructures on wettability. Although these studies differ in terms of study material, parameters, and wetting transitions, the overall trends of increased CAs and the presence of Cassie wetting states remain consistent.

Fig. 7(e) and (f) illustrates how the contact angles change with in relation to sample temperature for the silicone rubber surfaces having micropillar heights of D = 80 µm and D = 110 µm. The CA varies depending on pitch at −20 °C (D = 80 µm and 110 µm), whereas the CA of these same surfaces remains quite constant at ambient temperature (22 °C) (Fig. 7a, b, e, f). The observed CA of these surfaces at −20 °C is lower than that for surfaces at an ambient temperature. For the D = 80 µm series of surfaces, as pitch increases from 125 to 150 µm, the

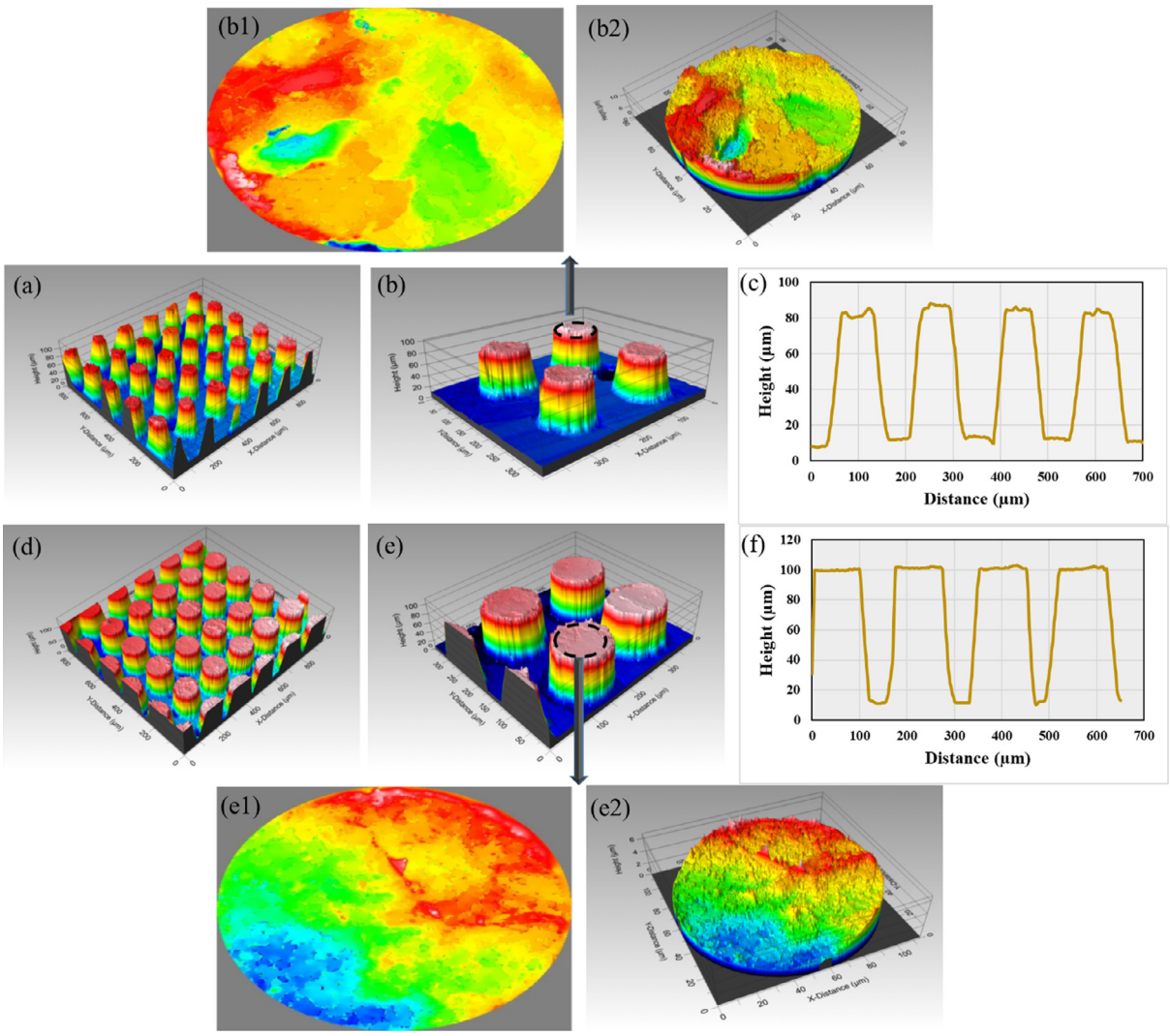

Fig. 6. A 3D profilometry image of microstructures (D = 80 µm, P = 175 µm) at a magnification of (a) 20×, (b) 50×, and (c) surface height map, (b1) top view of the pillar top (b2) 3D profile of the pillar top. Microstructures (D = 110 µm, P = 150 µm) at a magnification of (d) 20×, (e) 50×, and (f) surface height map, (e1) top view of the pillar top and (e2) 3D profile of the pillar top.

CA increases from 128° to 144°. As pillar spacing increases further to 225 µm, CA decreases to 122° because of ambient vapor condensation and frost formation, leading to a transition from a Cassie–Baxter to a Wenzel state (Fig. 8) (He et al., 2014, 2013; Hou et al., 2020b). For the D = 110 µm series of surfaces, increased pillar spacing (from 125 to 225 µm) produces a higher CA (maximum of 138° for P = 225 µm), followed by a lower CA as pitch increases further. Therefore, the morphology of the silicone surface has an obvious effect on CA at colder temperatures.

3.3. Freezing delay time

We conducted freezing delay time measurements on 13 samples to investigate the correlation between anti-icing properties and surface wettability and to evaluate the role of pillar diameter and pitch on ice nucleation time. Fig. 9 shows the water droplet shapes during crystallization.

Water droplets on patterned silicone rubber surfaces exhibit a longer ice nucleation time relative to those placed on a pristine silicone rubber at −20 °C (Fig. 10). The patterned silicone rubber produces higher water CAs and a therefore less contact area between the water droplet and surface, favoring a longer ice nucleation time. The pattern of pillars also allows air to form at the water–surface interface. By acting as an insulator, the entrapped air slows the heat exchange between the droplet and the surface (Chen et al., 2020; Maghsoudi et al., 2021; Keshavarzi et al., 2022a), thereby producing a longer delay in freezing.

Freezing delay is significantly enhanced for the patterned silicone rubber surfaces relative to pristine silicone rubber surfaces (about 80 s). For surfaces having a pillar diameter of 80 µm, we observe a freezing delay time of 272 s for surfaces having a 125 µm pitch, as the heat transfer is retarded by the presence of an underlying air layer and decreased water–solid contact area. This freezing delay reaches a maximum at a pitch of 150 µm (640 s), almost 8× that of a pristine surface. The longer freezing delay time can also be attributed to the higher Gibbs free energy barrier for a superhydrophobic surface than for a hydrophobic surface (Guo et al., 2021; Rahimi et al., 2016; Qi et al., 2020; Eberle et al., 2014). As the pillar pitch increases further, freezing delay decreases, illustrating that the Cassie–Baxter state can shift to a Wenzel state if pillar spacing increases sufficiently (here P >150 µm). This transition of wetting state influences surface hydrophobicity and droplet penetration among the microstructures; thus icephobicity is reduced as is ice nucleation time (Hou et al., 2020b; Bartolo et al., 2006; Oberli et al., 2014).

A similar pattern is observed for surfaces having pillars with a diameter of 110 µm (Fig. 10b). Ice nucleation time for the patterned silicone rubber surfaces increases from 255 to a maximum of 572 s as

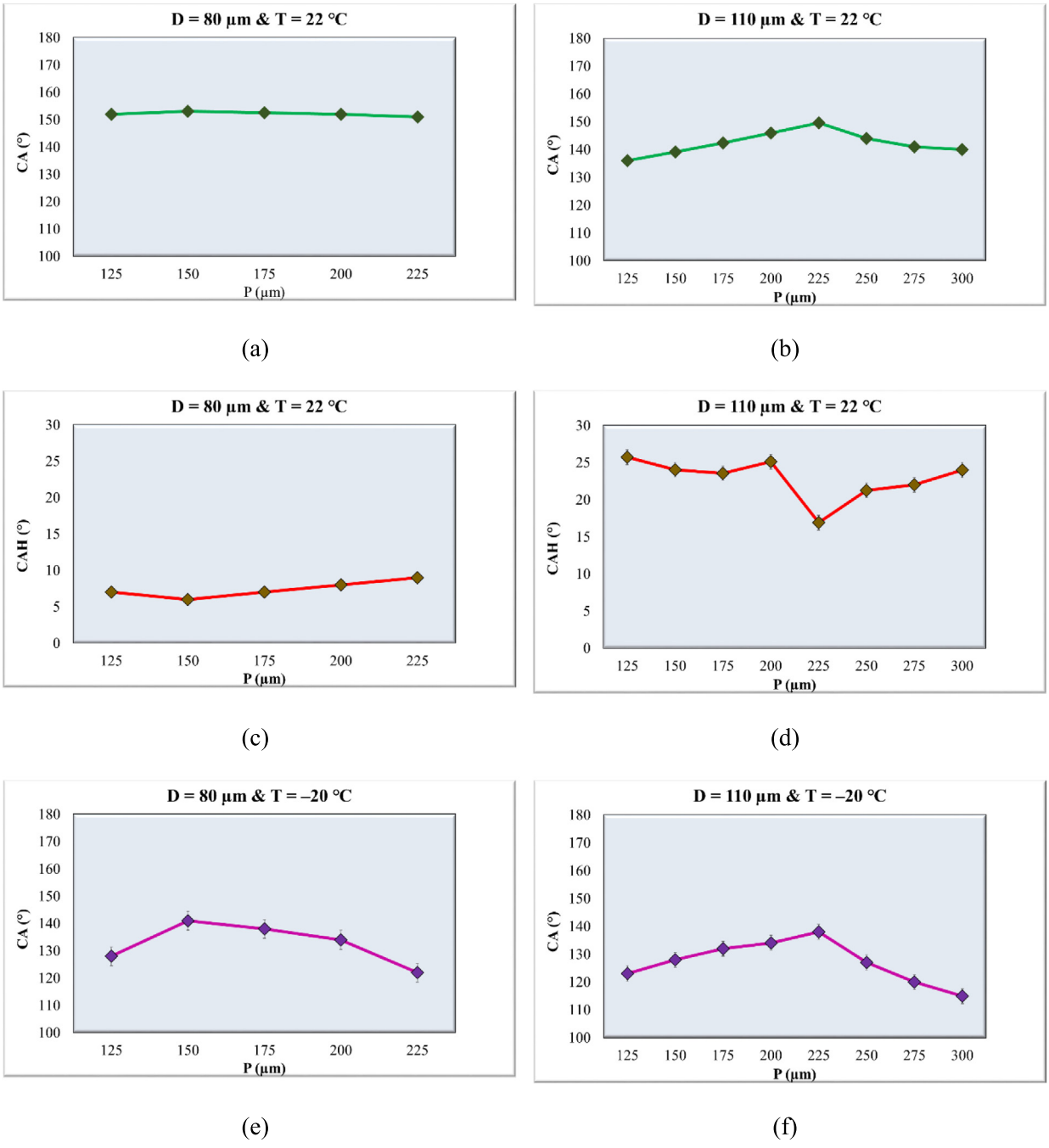

Fig. 7. Water contact angle (CA) and contact angle hysteresis (CAH) of the fabricated silicone rubber surfaces; (a) CA of D = 80 µm, T = 22 °C, (b) CA of D = 110 µm, T = 22 °C, (c) CAH of D = 80 µm, T = 22 °C, (d) CAH of D = 110 µm, T = 22 °C (e) CA of D = 80 µm, T = –20 °C, and (f) CA of D = 110 µm, T = –20 °C.

the spacing increases from 125 to 225 µm. Ice nucleation time drops sharply to 125 s as spacing increases further to 300 µm. This reduction at wider spacings indicates that the droplets embedded between the microstructures, ambient vapor condensation, and frost formation all reduce the ice nucleation time with a greater pillar spacing. As both the 80 µm and 110 µm pillar diameter surfaces are tested with droplets of the same size (10 µL), the transition in ice nucleation time beyond a critical threshold is most likely caused by the spacing factor and pillar diameter, which is directly related to the fractional solid–liquid contact area (Bhushan et al., 2007).

The ice nucleation times on the superhydrophobic surface with pillars of D = 80 µm are greater than for a hydrophobic surface having pillars of D = 110 µm, showing that surface structure influences droplet icing delay. Enhancing the anti-icing performance can be achieved by optimizing the superhydrophobic surface design to favor higher droplet CAs, increased amounts of trapped air, and, thus, a lower heat transfer efficiency during the cooling and freezing stages to extend freezing delay times.

Direct quantitative comparisons of ice nucleation times obtained in other studies can be challenging because of differences in the experimental facilities, the sensitivity of the process, droplet volume, humidity, temperature, and surface features. Chen et al. (2020) used a nanosecond fiber laser to texture silicone rubber surfaces and create superhydrophobic surfaces covered by various microstructures. These superhydrophobic surfaces displayed superior anti-icing properties and significantly delayed ice formation, with a water droplet of 9 µL requiring approximately 540 s to freeze at −18 °C. Additionally, the superhydrophobic surfaces exhibited excellent hydrophobic performance

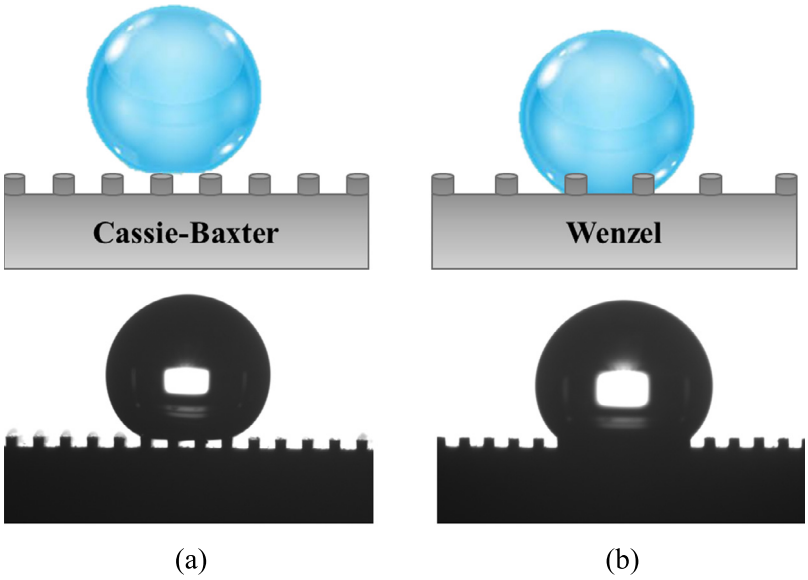

Fig. 8. Schematic illustration and photographs of the (a) at 22 °C, Cassie–Baxter and (b) at −20 °C, Wenzel state on patterned silicon rubber surfaces.

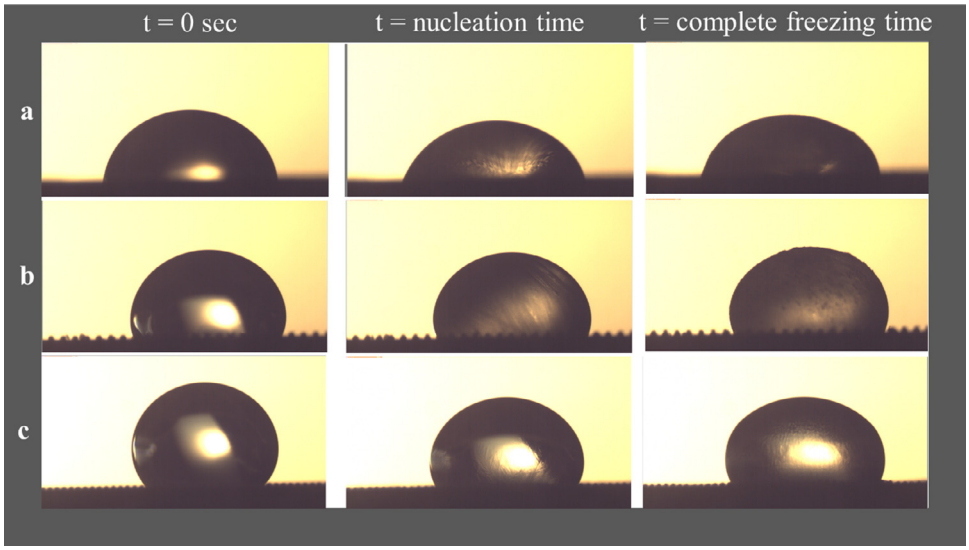

Fig. 9. Images of the freezing of a 10 μL droplet on various solid surfaces at −20 °C; (a) pristine silicone rubber, (b) a micropillar-covered surface with pillar dimensions of D = 110 μm, P = 275 μm; and (c) D = 75 μm, P = 175 μm.

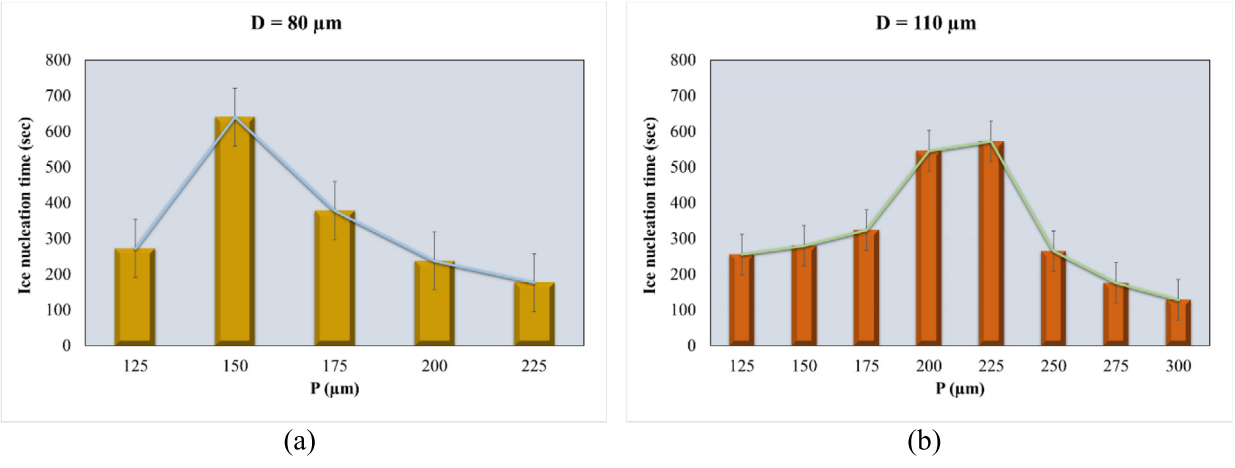

Fig. 10. Ice nucleation times for a 10 μL droplet placed on surfaces as a function of pitch (P) and pillar diameter (D); (a) D = 80 μm, (b) D = 110 μm, both at −20 °C.

at low temperatures. Nguyen et al. (2018) focused on the impact of texture parameters on passive anti-icing measures. They investigated the freezing time of water droplets on uniformly textured surfaces with different pillar top diameters (30–145 nm) and heights (300–575 nm). The maximum freezing time observed among the surfaces tested was for a 5 μL water droplet at −20 °C and humidity ≤5% at 49.2 s on a surface with pillars having a diameter of 30 nm, a height of 300 nm, and a spacing of 150 nm. Similarly, Li et al. (2020) observed a maximum ice nucleation time of 494 s for a 50 μL water droplet on an aluminum alloy at −13 °C and 53% humidity. This surface's microcylindrical structures had a diameter of 50 μm and a pitch of 100 μm.

These comparative insights confirm that our findings align with the general trend of enhanced ice nucleation delay on patterned surfaces. Moreover, our study conducted freezing delay time measurements on multiple samples (13 samples) differing in their pillar diameters and spacings. Although our study provides a comprehensive understanding of the relationship between surface morphology and ice nucleation time, further research is required to better understand the potential of patterned surfaces in enhancing anti-icing properties. The optimized design of superhydrophobic surfaces to promote higher droplet CA, increased trapped air, and reduced heat transfer efficiency during cooling and freezing stages hold promise for enhancing the anti-icing performance of micro-nanotextured surfaces.

4. Conclusion

In this study, we successfully used micromachining and direct replication via a compression molding method to develop a simple and effective method for designing and fabricating patterned microcylindrical surfaces on HTV silicone rubber. Our study of how micropillar geometry – pillar diameter and pitch – affects surface wettability and ice nucleation time provides valuable insights into the relationship between surface structures and anti-icing properties. Careful manipulation of microstructure geometry permits precise control over surface wettability and, consequently, the anti-icing/icephobic properties of the prepared surfaces.

The observed transition from Cassie to Wenzel wetting, influenced by pillar diameter and spacing, highlights the importance of microstructure design in achieving desired surface characteristics. We found that Cassie wetting occurs as the diameter decreases and the spacing between the microcylindrical pillars increases, whereas Wenzel wetting occurs once diameters and pillar spacing increase beyond a threshold value. The HTV silicone rubber surface demonstrated superhydrophobic wettability, with a CA ≥150° and a CAH <10°, when pillar diameter was 80 μm. Although all CAs were similar under ambient temperature, CAs decreased at −20 °C and showed greater variability in relation to pillar spacing. For the prepared micropillar-covered surfaces, we observed a maximum freezing delay time of 640 s at a pitch distance of 150 μm, almost 8× longer than for pristine silicone rubber surfaces. Surfaces having a pillar diameter of 110 μm produced a smaller CA and a larger CAH than surfaces with pillars having diameters of 80 μm; maximum CA was 149° at a pitch distance of 225 μm with a maximum ice nucleation time of 572 s.

These findings have significant implications for the development of materials having enhanced anti-icing properties. By tailoring the microstructure geometry, it becomes possible to create superhydrophobic surfaces that effectively delay ice nucleation. In conclusion, our study provides an easy means of altering the geometry of microcylindrical pillars to control the wetting and anti-icing properties of prepared surfaces.

CRediT authorship contribution statement

S. Keshavarzi: Conceptualization, Investigation, Methodology, Validation, Writing – original draft, Writing – review & editing. **B. Bouazara:** Conceptualization, Methodology, Software, Validation, Investigation, Writing – original draft, Writing – review & editing. **G. Momen:** Conceptualization, Project administration, Supervision, Resources, Funding acquisition, Writing – review & editing. **R. Jafari:** Conceptualization, Project administration, Supervision, Resources, Funding acquisition, Writing – review & editing.

Declaration of competing interest

The authors declare that they have no known competing financial interests or personal relationships that could have appeared to influence the work reported in this paper.

Data availability

Data will be made available on request.

Acknowledgments

The authors would like to acknowledge the financial support from Natural Sciences and Engineering Research Council of Canada (NSERC). We also thank Carol Mercier at the Anti-icing Materials International Laboratory (LIMA), UQAC, for helping develop the experimental setup.

References

Aldhaleai, A., Tsai, P.A., 2021. Langmuir 37 (1), 348–356. http://dx.doi.org/10.1021/acs.langmuir.0c02945.
Bartolo, D., Bouamrirene, F., Verneuil, É., Buguin, A., Silberzan, P., Moulinet, S., 2006. Europhys. Lett. 74 (2), 299–305. http://dx.doi.org/10.1209/epl/i2005-10522-3.
Bhushan, B., Chae Jung, Y., 2007. Ultramicroscopy 107 (10–11), 1033–1041. http://dx.doi.org/10.1016/j.ultramic.2007.05.002.
Bhushan, B., Nosonovsky, M., Chae Jung, Y., 2007. J. R. Soc. Interface 4 (15), 643–648. http://dx.doi.org/10.1098/rsif.2006.0211.
Brousseau, E.B., Dimov, S.S., Pham, D.T., 2010. Int. J. Adv. Manuf. Technol. 47 (1–4), 161–180. http://dx.doi.org/10.1007/s00170-009-2214-5.
Cassie, A.B.D., Baxter, S., 1944. Trans. Faraday Soc. 40, 546. http://dx.doi.org/10.1039/tf9444000546.
Chen, L., Ping, H., Yang, T., Hu, T., Bennett, P., Zheng, Z., Yang, Q., Perrie, W., Edwardson, S.P., Dearden, G., Liu, D., 2020. Mater. Res. Express 6 (12), 1250e2. http://dx.doi.org/10.1088/2053-1591/ab6542.
Chen, L., Wang, X., Yang, T., Ping, H., Bennett, P., Zheng, Z., Yang, Q., Perrie, W., Edwardson, S.P., Dearden, G., Liu, D., 2018. J. Phys. D. Appl. Phys. 51 (44), 445301. http://dx.doi.org/10.1088/1361-6463/aae13d.
Eberle, P., Tiwari, M.K., Maitra, T., Poulikakos, D., 2014. Nanoscale 6 (9), 4874–4881. http://dx.doi.org/10.1039/C3NR06644D.
Extrand, C.W., 2004. Langmuir 20 (12), 5013–5018. http://dx.doi.org/10.1021/la036481s.
Farzaneh, M., 2014. IEEE Trans. Dielectr. Electr. Insul. 21 (5), 1997–2011. http://dx.doi.org/10.1109/TDEI.2014.004598.
Gao, J., Zhao, J., Liu, L., Xue, W., 2016. Surf. Eng. 32 (2), 125–131. http://dx.doi.org/10.1179/1743294414Y.0000000431.
Guo, Z., Yang, F., 2018. Surfaces and Interfaces of Biomimetic Superhydrophobic Materials. Wiley-VCH Verlag GmbH & Co. KGaA, Weinheim, Germany, pp. 1–24.
Guo, C., Zhang, M., Hu, J., 2021. Colloids Surf. A Physicochem. Eng. Asp. 621 (February), 126587. http://dx.doi.org/10.1016/j.colsurfa.2021.126587.
He, Y., Jiang, C., Cao, X., Chen, J., Tian, W., Yuan, W., 2014. Appl. Surf. Sci. 305, 589–595. http://dx.doi.org/10.1016/j.apsusc.2014.03.139.
He, Y., Jiang, C., Wang, S., Yin, H., Yuan, W., 2013. Appl. Surf. Sci. 285, 682–687. http://dx.doi.org/10.1016/j.apsusc.2013.08.110.
Hopmann, C., Behmenburg, C., Recht, U., Zeuner, K., 2014. Silicon 6 (1), 35–43. http://dx.doi.org/10.1007/s12633-013-9164-0.
Hou, W., Shen, Y., Tao, J., Xu, Y., Jiang, J., Chen, H., Jia, Z., 2020a. Colloids Surf. A Physicochem. Eng. Asp. 586 (2019), 124180. http://dx.doi.org/10.1016/j.colsurfa.2019.124180.
Hou, W., Shen, Y., Tao, J., Xu, Y., Jiang, J., Chen, H., Jia, Z., 2020b. Colloids Surf. A Physicochem. Eng. Asp. 586, 124180. http://dx.doi.org/10.1016/j.colsurfa.2019.124180.
Hu, H.W., Tang, G.H., Niu, D., 2015. Int. J. Heat Mass Transfer http://dx.doi.org/10.1016/j.ijheatmasstransfer.2015.02.006.
Jeevahan, J., Chandrasekaran, M., Britto Joseph, G., Durairaj, R.B., Mageshwaran, G., 2018. J. Coatings Technol. Res. 15 (2), 231–250. http://dx.doi.org/10.1007/s11998-017-0011-x.
Jiang, J., Sheng, Q., Tang, G.H., Yang, M.Y., Guo, L., 2022. Int. J. Heat Mass Transfer 190, 122730. http://dx.doi.org/10.1016/j.ijheatmasstransfer.2022.122730.
Keshavarzi, S., Entezari, A., Maghsoudi, K., Momen, G., Jafari, R., 2022a. Cold Reg. Sci. Technol. 203, 103659. http://dx.doi.org/10.1016/j.coldregions.2022.103659.

Keshavarzi, S., Sourati, J., Momen, G., Jafari, R., 2022b. Int. J. Heat Mass Transfer 195, 123190. http://dx.doi.org/10.1016/j.ijheatmasstransfer.2022.123190.

Li, X., Wang, G., Moita, A.S., Zhang, C., Wang, S., Liu, Y., 2020. Appl. Surf. Sci. http://dx.doi.org/10.1016/j.apsusc.2019.144386.

Liu, X., Wu, W., Wang, X., Luo, Z., Liang, Y., Zhou, F., 2009. Soft Matter 5 (16), 3097. http://dx.doi.org/10.1039/b902973g.

Ma, M., Hill, R.M., 2006. Curr. Opin. Colloid Interface Sci. 11 (4), 193–202. http://dx.doi.org/10.1016/j.cocis.2006.06.002.

Maghsoudi, K., Momen, G., Jafari, R., Farzaneh, M., 2018. Appl. Surf. Sci. 458, 619–628. http://dx.doi.org/10.1016/j.apsusc.2018.07.099.

Maghsoudi, K., Vazirinasab, E., Jafari, R., Momen, G., 2020a. Mater. Manuf. Process. 35 (14), 1567–1575. http://dx.doi.org/10.1080/10426914.2020.1779942.

Maghsoudi, K., Vazirinasab, E., Momen, G., Jafari, R., 2020b. Ind. Eng. Chem. Res. 59 (20), 9343–9363. http://dx.doi.org/10.1021/acs.iecr.0c00508.

Maghsoudi, K., Vazirinasab, E., Momen, G., Jafari, R., 2021. J. Mater Process. Technol. 288, 116883. http://dx.doi.org/10.1016/j.jmatprotec.2020.116883.

Matsumura, T., Iida, F., Hirose, T., Yoshino, M., 2012. J. Mater Process. Technol. 212 (12), 2669–2677. http://dx.doi.org/10.1016/j.jmatprotec.2012.05.021.

Nayak, B.K., Caffrey, P.O., Speck, C.R., Gupta, M.C., 2013. Appl. Surf. Sci. 266, 27–32. http://dx.doi.org/10.1016/j.apsusc.2012.11.052.

Nguyen, T.-B., Park, S., Lim, H., 2018. Appl. Surf. Sci. 435, 585–591. http://dx.doi.org/10.1016/j.apsusc.2017.11.137.

Oberli, L., Caruso, D., Hall, C., Fabretto, M., Murphy, P.J., Evans, D., 2014. Adv. Colloid Interface Sci. 210, 47–57. http://dx.doi.org/10.1016/j.cis.2013.10.018.

Öner, D., McCarthy, T.J., 2000. Langmuir 16 (20), 7777–7782. http://dx.doi.org/10.1021/la000598o.

Pratap, T., Patra, K., 2018. Surf. Coatings Technol. 349, 71–81. http://dx.doi.org/10.1016/j.surfcoat.2018.05.056.

Qi, Y., Yang, Z., Chen, T., Xi, Y., Zhang, J., 2020. Appl. Surf. Sci. 501 (2019), 144165. http://dx.doi.org/10.1016/j.apsusc.2019.144165.

Rahimi, M., Afshari, A., Thormann, E., 2016. ACS Appl. Mater. Interfaces 8 (17), 11147–11153. http://dx.doi.org/10.1021/acsami.6b02321.

Robin H.A. Ras, A.M., 2016. Non-Wettable Surfaces: Theory, Preparation and Applications.

Shen, Y., Wu, X., Tao, J., Zhu, C., Lai, Y., Chen, Z., 2019. Prog. Mater. Sci. 103 (February), 509–557. http://dx.doi.org/10.1016/j.pmatsci.2019.03.004.

Subhash Latthe, S., Basavraj Gurav, A., Shridhar Maruti, C., Shrikant Vhatkar, R., 2012. J. Surf. Eng. Mater. Adv. Technol. 02 (02), 76–94. http://dx.doi.org/10.4236/jsemat.2012.22014.

Tourkine, P., Le Merrer, M., Quéré, D., 2009. Langmuir 25 (13), 7214–7216. http://dx.doi.org/10.1021/la900929u.

Weng, C., Yang, J., Wang, F., Ding, T., Zhai, Z., 2019. J. Polym. Eng. 40 (1), 86–97. http://dx.doi.org/10.1515/polyeng-2019-0109.

Wenzel, R.N., 1949. J. Phys. Colloid Chem. 53 (9), 1466–1467. http://dx.doi.org/10.1021/j150474a015.

Zhang, X., Shi, F., Niu, J., Jiang, Y., Wang, Z., 2008. J. Mater. Chem. 18 (6), 621–633. http://dx.doi.org/10.1039/B711226B.

Zhou, M., Xiong, X., Jiang, B., Weng, C., 2018. Appl. Surf. Sci. 427, 854–860. http://dx.doi.org/10.1016/j.apsusc.2017.08.003.